JOURNAL OF SPACECRAFT AND ROCKETS
Vol. 38, No. 4, July–August 2001

Theoretical and Experimental Modeling of Real Projectile Flight Heating

Friedrich Seiler,* Udo Werner,† and Gunther Patz‡
French–German Research Institute of Saint-Louis, F-68301 Saint-Louis, France

A projectile with a conical nose flying at Mach number $M_\infty > 1$ in the atmosphere develops a bow shock around its nose by which the incoming airflow is turned parallel to the projectile surface. Across the shock wave, the air is compressed, heated, and accelerated from upstream air pressure p_∞, upstream air temperature T_∞, and u_∞, which is equal to the projectile flight velocity u_p, to the downstream parameters p_e, T_e, and u_e. Consequently, a heat flux develops from the hot airflow along the projectile surface which is directed into the projectile material. This heat flux causes a temperature increase that depends on the projectile speed, the flight time, the structure of the surface material, and its geometry. A boundary-layer model is applied, and the gas heat flux into the projectile nose cone is analytically determined. To predict the heating of the solid projectile cone, an analytical solution, coming from the heat conduction equation, is used to obtain the surface temperature distribution. Experimentally the projectile flight in the atmosphere is modeled in a worldwide unique aerothermoballistic high-pressure facility built at the French–German Research Institute of Saint-Louis, where the heating during several seconds of atmospheric flight is duplicated with a flight in compressed gas resulting in the same heat flux for a flight time of some milliseconds. In this facility the cone surface temperature is measured by detecting the intensity of the infrared emission coming from the cone surface.

Nomenclature

a_f	=	transfer factor
B	=	function of n
c	=	heat capacity of projectile material
c_D	=	drag of projectile
c_p	=	heat capacity of gas flow
n	=	constant factor
Pr	=	Prandt number
p	=	static gas pressure
$\dot{q}$	=	heat flux
r, ϑ, φ	=	spherical coordinates
T	=	gas temperature
T_r	=	recovery temperature
t	=	time
u, v	=	velocity components
x, y	=	Cartesian coordinates
δ	=	boundary-layer thickness
δ^{**}	=	momentum thickness
λ	=	projectile material thermal conductivity
ν	=	kinematic viscosity
μ	=	dynamic viscosity
ρ	=	gas density
τ	=	skin friction
φ	=	factor concerning gas compressibility

Subscripts

c	=	flow around cone
e	=	flow outside of boundary layer
g	=	gas flow
p	=	projectile
w	=	cone surface
∞	=	flow upstream of bow shock

Introduction

THE aim of our work is to model theoretically and experimentally the heating of a projectile as it appears during its hypersonic flight in Earth's atmosphere. By bow shock heating an extreme heat flux develops toward the projectile surface, followed by high surface temperatures. In this study, the temperature increase at the nose of these hypersonic projectiles is investigated.

Surface temperature measurements in flight are very difficult to carry out. For this purpose a special ground-test facility was built, which consists of a preaccelerator and a test tube into which the projectile under investigation is injected. After injection, the sharp-nosed body is flying at supersonic velocity in compressed gas, for example, air or nitrogen at ambient temperature. The facility, developed at the French–German Research Institute of Saint-Louis (ISL), is unique worldwide and is called an aerothermoballistic high-pressure facility.

Using a similarity law, the heating for a flight in the atmosphere at condition (1) and the flight in the test tube at condition (2) can be related to each other by the following relation:

$$p_1 f_1(u_1, t_1) = p_2 f_2(u_2, t_2) \tag{1}$$

The two functions f_1 and f_2 depend on the flight histories $u_1(t_1)$ and $u_2(t_2)$, as well as on the flight times t_1 and t_2. The parameter p_1 is the pressure in the atmosphere, and p_2 is that in the test facility. By bow shock compression, the incoming flow is heated and directed parallel to the nose cone surface of the projectile, as shown in Fig. 1, in the reference frame of the projectile. At the cone surface, a turbulent boundary layer develops, as shown in Fig. 2, according to the existent wall boundary conditions w and those at the outer edge of the boundary layer, e for the flow velocity and gas temperature.

For calculation purposes, usually, the whole conservation equations of mass, momentum, and energy have to be taken into account, including skin friction and heat conduction. Numerical methods have to be used to solve this complex system of differential equations. In this study, a fast running procedure was developed to find solutions from the conservation equations for the boundary-layer formation at the surface of a projectile in flight. We used the boundary layer estimation of Prandtl (see Ref. 1) to get solutions in terms of analytical relations, which are described in the next section.

Theoretical Description

Boundary-Layer Prediction

In airflows at very high Reynolds numbers, a thin boundary layer develops at the surface cone of the projectile forebody (cone shape). Herein, viscosity and heat conduction are important factors, and the boundary-layer theory can be applied for cone flow prediction.

Received 25 July 2000; revision received 3 February 2001; accepted for publication 10 April 2001.

*Professor, Shock Tube Department, 5, Rue du Général Cassagnou.
†Research Scientist, Accelerator Department, 5, Rue du Général Cassagnou.
‡Senior Scientist, Shock Tube Department, 5, Rue du Général Cassagnou.

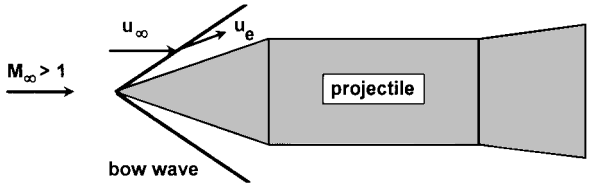

Fig. 1 Bow wave development in supersonic flow.

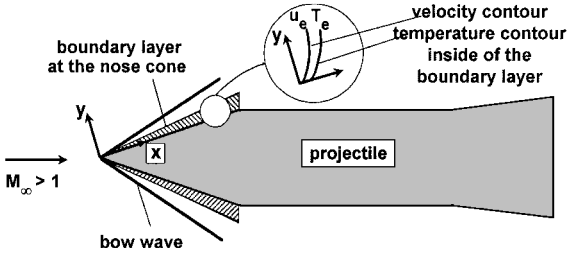

Fig. 2 Boundary layer at the nose cone.

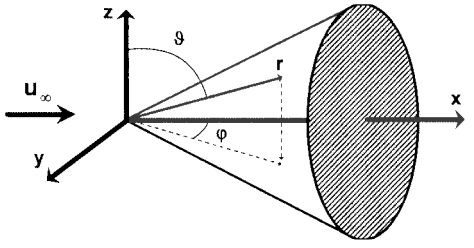

Fig. 3 Projectile's nose in spherical coordinates.

Across this layer, the velocity increases from zero at the cone surface to the velocity u_e outside. The gas temperature changes from temperature T_w at the surface of the projectile nose to the gas temperature T_e at the border of the boundary layer, formed at the nose cone of the projectile behind the bow wave existing in supersonic flow as shown in the schematic of Fig. 2.

For a theoretical description of the formation of the boundary layer considered herein, the discussed system of conservation equations containing the mass, momentum, and energy equations have to be applied. Furthermore, due to high Reynolds number, the airflow is turbulent, and a turbulence model must be fitted into this set of equations. It is difficult to find a theoretical solution for this complex system of differential equations, and in most cases the solution must be found numerically. An analytical solution is sometimes less exact than the solution of the full set of conservation equations, but illustrates the influence of important parameters. Therefore, a scheme for solving analytically Prandtl's boundary-layer equations has been developed for predicting the formation of the turbulent boundary layer at the surface of the projectile nose cone. The boundary-layer equations are considered in spherical coordinates with its origin located at the tip of the projectile's nose (Fig. 3). Because the boundary layer becomes turbulent, the parameters considered in the conservation equations are written as time-averaged mean values $\bar{\rho}$, $\bar{u}$, $\bar{v}$, and $\bar{T}$. The projectile flight speed history during atmospheric flight will be approximated with a time-step procedure.[2] In this analysis, the flow around the cone is treated as stepwise time independent and so the time dependence is not considered in Prandtl's boundary-layer equations. In spherical coordinates, r, ϑ, and φ, this set of differential equations[1] is written as follows.

Mass:

$$\frac{\partial}{\partial r}(\bar{\rho}\bar{u}) + \frac{1}{r}\frac{\partial}{\partial \vartheta}(\bar{\rho}\bar{v}) + \frac{2}{r}(\bar{\rho}\bar{u}) = 0 \tag{2}$$

Momentum:

$$\bar{\rho}\bar{u}\frac{\partial \bar{u}}{\partial r} + \frac{1}{r}\bar{\rho}\bar{v}\frac{\partial \bar{u}}{\partial \vartheta} = \frac{1}{r^2}\frac{\partial}{\partial \vartheta}\left(\mu\frac{\partial \bar{u}}{\partial \vartheta}\right) \tag{3}$$

Energy:

$$\bar{\rho}\bar{u}\frac{\partial}{\partial r}(c_p\bar{T}) + \frac{1}{r}\bar{\rho}\bar{v}\frac{\partial}{\partial \vartheta}(c_p\bar{T}) = \frac{1}{r^2}\frac{\partial}{\partial \vartheta}\left(\lambda\frac{\partial \bar{T}}{\partial \vartheta}\right) + \frac{1}{r^2}\mu\left(\frac{\partial \bar{u}}{\partial \vartheta}\right)^2 \tag{4}$$

The differential equations (2–4) have to be solved using the boundary conditions in Eqs. (5) for temperature T and velocity components $\bar{u}$ and $\bar{v}$:

$$\bar{T}(r, \vartheta_c) = T_c \tag{5a}$$

$$\bar{T}(r, \vartheta_w) = T_w \tag{5b}$$

$$\bar{u}(r, \vartheta_c) = u_c \tag{5c}$$

$$\bar{u}(r, \vartheta_w) = 0 \tag{5d}$$

$$\bar{v}(r, \vartheta_w) = 0 \tag{5e}$$

For finding a solution, Eqs. (2–4) are transformed with the following relations:

$$\tilde{\chi} = \sqrt{3}[r(\vartheta - \vartheta_w)/\sqrt{r}] \tag{6a}$$

$$\bar{v} = \sqrt{3}/\sqrt{r}\left\{\bar{w}(\tilde{\chi}) - \tfrac{2}{3}\tilde{\chi}\bar{u}\right\} \tag{6b}$$

When Eqs. (6a) and (6b) are introduced in Eqs. (2–4) a new set of differential equations results. This procedure is explained in detail by Hantzsche and Wendt.[3]

Mass:

$$-\frac{\tilde{\chi}}{2}\frac{\mathrm{d}}{\mathrm{d}\tilde{\chi}}(\bar{\rho}\bar{u}) + \frac{\mathrm{d}}{\mathrm{d}\tilde{\chi}}(\bar{\rho}\bar{w}) = 0 \tag{7}$$

Momentum:

$$-\frac{\bar{\rho}\bar{u}\tilde{\chi}}{2}\frac{\partial \bar{u}}{\partial \tilde{\chi}} + \bar{\rho}\bar{w}\frac{\partial \bar{u}}{\partial \tilde{\chi}} = \frac{\partial}{\partial \tilde{\chi}}\left(\mu\frac{\partial \bar{u}}{\partial \tilde{\chi}}\right) \tag{8}$$

Energy:

$$-\frac{\bar{\rho}\bar{u}\tilde{\chi}}{2}\frac{\partial}{\partial \tilde{\chi}}(c_p\bar{T}) + \bar{\rho}\bar{w}\frac{\partial}{\partial \tilde{\chi}}(c_p\bar{T}) = \frac{\partial}{\partial \tilde{\chi}}\left(\lambda\frac{\partial \bar{T}}{\partial \tilde{\chi}}\right) + \mu\left(\frac{\partial \bar{u}}{\partial \tilde{\chi}}\right)^2 \tag{9}$$

From a formal point of view, Eqs. (7–9) are similar to the boundary-layer equations valid for the flat plate boundary layer. In this case, the simplified conservation equations are given for the two-dimensional plate geometry in Cartesian coordinates (Fig. 4) as follows.

Mass:

$$\frac{\partial}{\partial x}(\bar{\rho}\bar{u}) + \frac{\partial}{\partial y}(\bar{\rho}\bar{v}) = 0 \tag{10}$$

Momentum:

$$\bar{\rho}\bar{u}\frac{\partial \bar{u}}{\partial x} + \bar{\rho}\bar{v}\frac{\partial \bar{u}}{\partial y} = \frac{\partial}{\partial y}\left(\mu\frac{\partial \bar{u}}{\partial y}\right) \tag{11}$$

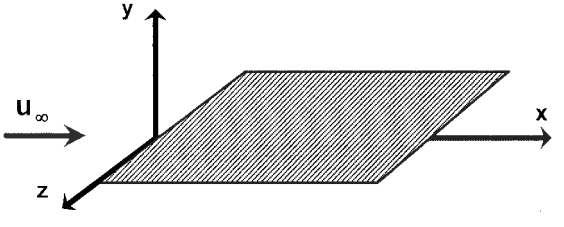

Fig. 4 Flat plate in Cartesian coordinates.

Energy:

$$\bar{\rho}\bar{u}\frac{\partial}{\partial x}(c_p\bar{T}) + \bar{\rho}\bar{v}\frac{\partial}{\partial y}(c_p\bar{T}) = \frac{\partial}{\partial y}\left(\lambda\frac{\partial\bar{T}}{\partial y}\right) + \mu\left(\frac{\partial\bar{u}}{\partial y}\right)^2 \quad (12)$$

Transforming the plate boundary layer Eqs. (10–12) with

$$\chi = y/\sqrt{x} \quad (13a)$$

$$\bar{v} = \tilde{\bar{v}}/\sqrt{x} \quad (13b)$$

gives the following new set of boundary-layer equations describing the boundary-layer formation on a flat plate as follows.

Mass:

$$-\frac{\chi}{2}\frac{\mathrm{d}}{\mathrm{d}\chi}(\bar{\rho}\bar{u}) + \frac{\mathrm{d}}{\mathrm{d}\chi}(\bar{\rho}\tilde{\bar{v}}) = 0 \quad (14)$$

Momentum:

$$-\frac{\bar{\rho}\bar{u}\chi}{2}\frac{\partial\bar{u}}{\partial\chi} + \bar{\rho}\tilde{\bar{v}}\frac{\partial\bar{u}}{\partial\chi} = \frac{\partial}{\partial\chi}\left(\mu\frac{\partial\bar{u}}{\partial\chi}\right) \quad (15)$$

Energy:

$$-\frac{\bar{\rho}\bar{u}\tilde{\chi}}{2}\frac{\partial}{\partial\chi}(c_p\bar{T}) + \bar{\rho}\tilde{\bar{v}}\frac{\partial}{\partial\chi}(c_p\bar{T}) = \frac{\partial}{\partial\chi}\left(\lambda\frac{\partial\bar{T}}{\partial\chi}\right) + \mu\left(\frac{\partial\bar{u}}{\partial\chi}\right)^2 \quad (16)$$

Regarding the transformed set of boundary-layer equations (7–9) for the cone boundary layer and Eqs. (14–16) for the plate boundary layer, we see that both systems appear to be equal. However, the difference between them can be found in the different meaning of the coordinates χ for the plate and $\tilde{\chi}$ for the cone. There are also differences in the velocity component definitions of $\tilde{\bar{v}}$ (plate) and $\bar{w}$ (cone).

The similarity between the transformed cone boundary layer equations (7–9) and those for the plate boundary layer [Eqs. (14–16)] shows that with a solution for the plate boundary-layer formation and the coordinate transformations, Eqs. (6) and (13), the cone boundary layer and the plate boundary layer can be related to each other. Hantzsche and Wendt[3] gave some data on these relations concerning laminar boundary-layer development. In our case, the flow is turbulent, and the transfer factor was determined with experimental data given by Chien.[4]

From considerations on the similarity between the cone and plate boundary-layer equations, it is justified to solve the plate boundary-layer equations (10–12) instead of the more complex cone boundary-layer equations (2–4). However, the results must be transformed to the given cone geometry by appropriate transfer data.[4]

A solution for the plate boundary-layer equations (10), (11), (12) can be found by Schlichting and Gersten,[1] that is, by determining some integral data that are obtained by integration of the boundary-layer equations along the coordinate y inside of the boundary-layer thickness. Integration of the momentum equation (11) from $y = 0$ (wall) up to $y = \delta$ (outer border of the boundary layer) gives

$$\int_{y=0}^{\delta}\left(\bar{\rho}\bar{u}\frac{\partial\bar{u}}{\partial x} + \bar{\rho}\bar{v}\frac{\partial\bar{u}}{\partial x}\right)\mathrm{d}y = \tau_w \quad (17)$$

with

$$\tau_w = \mu\left(\frac{\partial\bar{u}}{\partial y}\right)_w \quad (18)$$

When the velocity component $\bar{v}$ is replaced in Eq. (17) using the conservation equation of mass (10), then for the wall shear stress τ_w along the plate's coordinate x, the following differential equation is obtained, in which the flow parameters are integrated inside of the boundary layer from $y = 0$ to $y = \delta$ (Ref. 5):

$$\tau_w = \frac{\mathrm{d}}{\mathrm{d}x}\int_0^{\delta}\rho\bar{u}(\bar{u}_e - \bar{u})\,\mathrm{d}y + \frac{\mathrm{d}u_e}{\mathrm{d}x}\int_0^{\delta}(\rho_e\bar{u}_e - \rho\bar{u})\,\mathrm{d}y \quad (19)$$

In turbulent boundary layers, velocity profiles are described approximately by the power-law equation, as discussed by Schlichting and Gersten,[1]

$$\bar{u}/\bar{u}_e = (y/\delta)^{1/n}, \qquad 5 \le n \le 10 \quad (20)$$

When Eq. (20) is introduced into Eq. (19), a differential equation for the boundary-layer thickness δ as a function of x along the plate is obtained:

$$\frac{\mathrm{d}\delta}{\mathrm{d}x} = \frac{\delta}{\delta^{**}}B(n)\left(\frac{\nu_e}{\bar{u}_e\delta}\right)^{2/(n+1)} \quad (21)$$

This differential equation is solved with the outer core flow conditions e, that is, flow speed u_e, pressure p_e, and temperature T_e, giving the boundary-layer thickness $\delta(x)$. With $\tau_w = \tau_w(\delta)$ (Ref. 5) and using the Reynolds analogy as

$$\dot{q}_g = \left[c_p(\bar{T}_r - \bar{T}_w)Pr^{-\frac{2}{3}}\big/\bar{u}_e\right]\tau_w \quad (22)$$

the analytical solution for predicting the heat flux $\dot{q}_g$ at the surface as a function of the coordinate x along the cone surface of the projectile is given as

$$\dot{q}_g(x) = a_f(n+1)/(n+3)^{2/(n+3)}[B(n)\varphi]^{(n+1)/(n+3)}c_p(T_r - T_w)$$
$$Pr^{-\frac{2}{3}}\rho_e(\delta^{**}/\delta)^{2/(n+3)}\ \bar{u}_e^{(n+1)/(n+3)}(\nu_e/x)^{2/(n+3)} \quad (23)$$

All of the parameters used in Eq. (23), such as n, $B(n)$, φ, δ, δ^{**}, T_r, T_w, c_p, ρ_e, and ν_e, are defined in the Nomenclature and in more detail by Seiler.[6] To take into account the heat flux $\dot{q}_g$ for the sharp-cone geometry of the projectile nose, the calculated flat-plate heat flux of Eq. (23) is transformed to cone geometry using the transfer factor a_f. A theoretical estimation of this factor is not available for turbulent flows. To determine a_f, the heat flux $\dot{q}_g$ Eq. (23) is fitted to the experimental heat transfer results of Chien,[4] which were obtained at hypersonic flow conditions, as in this study. The experiments of Chien[4] have been performed in a wind tunnel using a sharp cone with a five-deg cone half-angle at a freestream Mach number $M_\infty = 7.9$. The best agreement with Eq. (23) is found with $a_f = 1.07$ using $n = 9$.

Heat Conduction Equation

The heat flux $\dot{q}_g(x)$ calculated from Eq. (23) is found to be practically less depending on the cone's coordinate x. Therefore, the one-dimensional heat conduction equation was applied inside the wall region (depth y) at each location x along the cone surface:

$$\frac{\partial\bar{T}}{\partial t} = k\frac{\partial^2\bar{T}}{\partial y^2}, \qquad \text{with} \qquad k = \frac{\lambda}{\rho c} \quad (24)$$

By integration of Eq. (24) with the given boundary conditions, an analytical solution for the temperature change ΔT_w at the cone as a function of the heat flux $\dot{q}_w(x)$ can be obtained as

$$\Delta T_w(x, y, t) = F/\sqrt{\rho c\lambda}$$
$$\times\,[2(\sqrt{t}/\sqrt{\pi})\exp(-y^2/4kt) - (y/\sqrt{k})\,\mathrm{erfc}(y/2\sqrt{kt})] \quad (25)$$

The analytical solution (25) is applied for calculating the temperature distribution $T_w(x, y, t)$ inside of the projectile nose as a function of the heat flux $\dot{q}_g(x)$. When $\dot{q}_g(x)$ of Eq. (23) is introduced

in Eq. (25) by assuming that the heat flux at the surface at $y = 0$ is equal for both the gas and the wall side, with

$$F = \dot{q}_g(x) = \dot{q}_w(x, y = 0) \tag{26}$$

the temperature distribution

$$T_w(x, y, t) = T_0 + \Delta T_w(x, y, t) \tag{27}$$

inside the nose cone material can be calculated.

Heating of Projectile Nose Cone

With the procedure described, different flight scenarios have been calculated to demonstrate the range of temperature increase at the nose for a projectile in real atmospheric flight scenario. Four projectile types are considered, with the masses m and drag c_D as follows: 1) high-speed German hypervelocity projectile (HFK), $m = 120$ kg and $c_D = 0.35$; 2) 120-mm kinetic energy projectile (KE), $m = 4$ kg and $c_D = 0.35$; 3) 30-mm full caliber projectile, $m = 360$ g and $c_D = 0.20$; and 4) 155-mm full caliber projectile, $m = 45$ kg and $c_D = 0.20$.

The flight trajectory was calculated for each of the four projectile types with the assumption of constant projectile drag c_D. The result for the projectile speed u_p vs flight time is given in Fig. 5 with two time coordinates. The upper one is valid for the HFK projectile, the KE projectile, and the 30-mm full caliber projectile, the lower one is valid only for the 155-mm full caliber projectile.

In Fig. 6, the predicted cone surface temperature variation at location $r = 10$ mm upstream of the cone tip is shown as a function of the flight time for the four projectile types considered. For all cases, it is assumed that the nose is made of steel with density $\rho = 7840$ kg/m^3, heat capacity $c = 458$ J/kg K, and heat conduction $\lambda = 50$ W/m K. For the HFK projectile, a maximum temperature of about 940 K is reached after a flight time of 2 s. The 120-mm subcaliber KE projectile is heated to about 650 K during 4-s flight time. A lower surface temperature is calculated for the 30-mm full caliber projectile. We obtain from Fig. 6 a maximum temperature of 420 K after 1-s flight. The 155-mm caliber projectile maximum cone surface temperature is in the range of 350 K after a flight of 3 s.

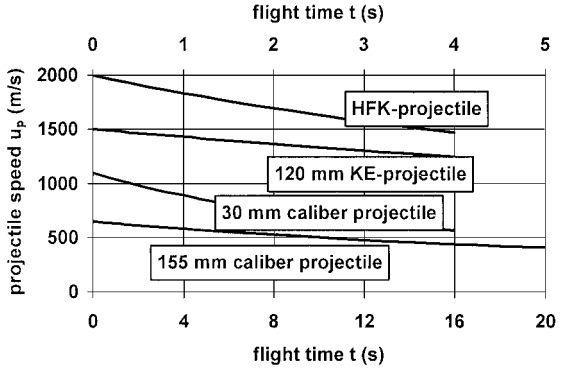

Fig. 5 Projectile speed scenarios vs flight time.

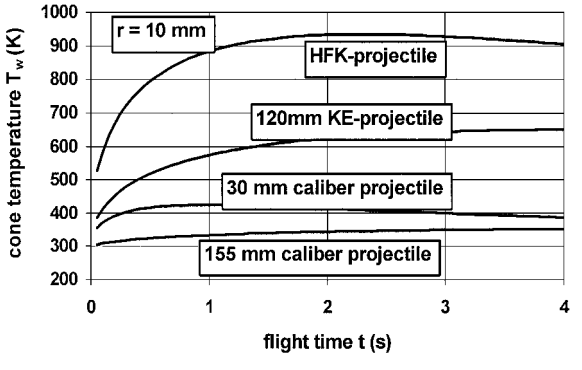

Fig. 6 Nose temperature at $r = 10$ mm from nose tip.

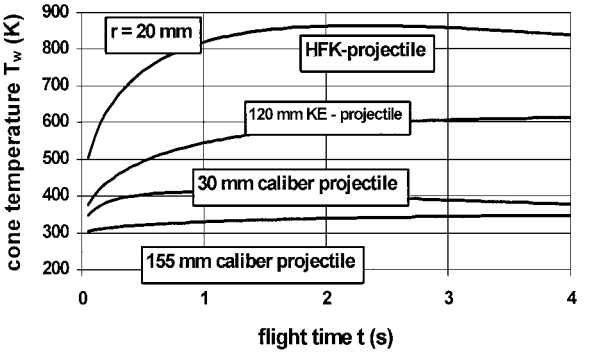

Fig. 7 Nose temperature at $r = 20$ mm from nose tip.

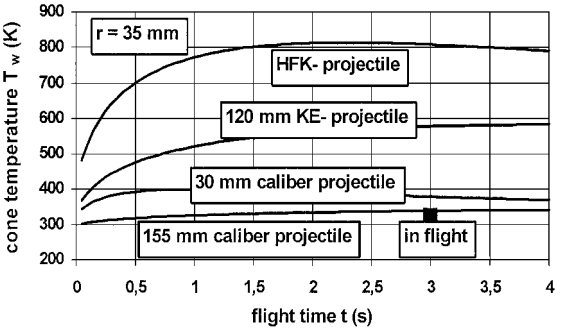

Fig. 8 Nose temperature at $r = 35$ mm from nose tip.

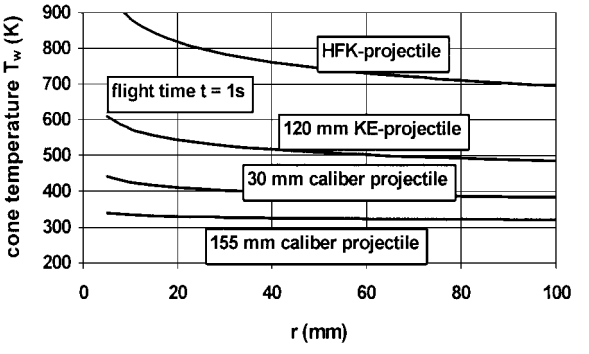

Fig. 9 Nose temperature at flight time $t = 1$ s.

Similar temperature histories develop for the position $r = 20$ mm upstream from the nose tip (Fig. 7), as well as for $r = 35$ mm (Fig. 8). Additionally, in Fig. 8 the result of a thermocouple measurement in flight is introduced for the 155-mm full caliber projectile.[7] The temperature measured is in very good agreement with the theoretical prediction. It must be taken into account that the thermocouple was not made of steel, which was used for calculating the cone heating. Therefore, some differences between measurement and theory must appear.

The temperature distribution along the cone surface is given in Fig. 9 for a flight time of 1 s. We see, as already discussed, the temperature development for the strongly heated HFK projectile nose, for the KE projectile, the 30-mm caliber projectile, and (lowest) the 155-mm full caliber projectile. The outcome of Fig. 9 shows that the temperature increases toward the nose tip to infinity for $r = 0$, which is theoretically given by the boundary-layer theory.

Transformation Equation

The goal of our investigations is to model the heat flux present in flight in the aerothermoballistic high-pressure facility, at the nose of a projectile. Relating the real flight condition (1) and the modeling conditions in our test facility (2) with Eq. (23) requires the condition of equal integral heat flux during the flight time t:

$$\int_{t=0}^{t} \dot{q}_{g,1}(x)\,\mathrm{d}t = \int_{t=0}^{t} \dot{q}_{g,2}(x)\,\mathrm{d}t \tag{28}$$

Then, for different flight cycles in the atmosphere at condition (1) and in our ground-testing facility at condition (2), relation (28) can be fulfilled if the condition in Eq. (1), namely,

$$p_1 f_1(u_1, t_1) = p_2 f_2(u_2, t_2)$$

for pressure p_1 and p_2, as well as for the functions f_1 and f_2, is balanced. The functions f_1 and f_2 must be calculated stepwise in time from Eq. (23) (Ref. 2). In case of constant projectile speeds u_1 and u_2, Eq. (1) evaluates as

$$p_1 \sqrt{t_1} = p_2 \sqrt{t_2} \tag{29}$$

However, the exact conditions for operation of the aerothermoballistic ground-testing facility, that is, gas pressure p_2 and test-flight time t_2, must be calculated according to the exact relation, Eq. (1), using the given atmospheric pressure p_1 and the real flight cycle t_1.

Experimental Modeling

Aerothermoballistic High-Pressure Facility

In the aerothermoballistic ground-testing facility, the bow wave heating at the nose of a projectile, flying for several seconds t_1 some kilometers in the lower atmosphere at $p_1 \approx 0.1$ MPa (normal pressure), can be modeled in compressed gas at p_2 with a flight time t_2 of some milliseconds. This facility consists of a powder gun for accelerating the projectiles to a muzzle velocity up to 2000 m/s, followed by a test tube into which the projectile models are injected (Fig. 10).

The test tube is placed between the two damp tanks, seen in Fig. 10, with all of the equipment necessary for operation: 1) valves for gas filling, 2) pressure gauges for wall pressure measurement, and 3) electromagnetic sensors for determination of projectile position. The compression tube has a length of about 5 m and is closed by diaphragms at both ends. A detailed description of the facility is given by Seiler et al.[8] The test tube is designed as a two-caliber tube with five inner rails for projectile guiding and is filled with compressed gas in the range of 2 MPa and higher. The outer caliber is 44 mm, and the inner rail caliber is 30 mm. A cross section of this high-pressure rail tube is given in Fig. 11. In the decelerator tube

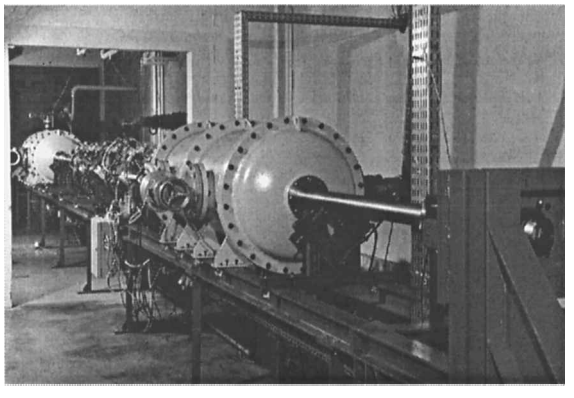

Fig. 10 Powder gun, two tanks, and rail tube in between.

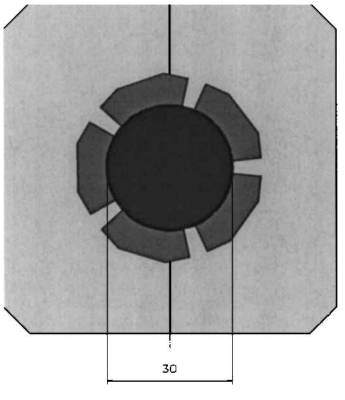

Fig. 11 Cross section of rail test tube with five rails.

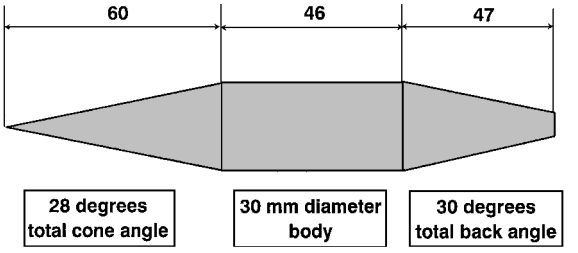

Fig. 12 Geometry of projectile used.

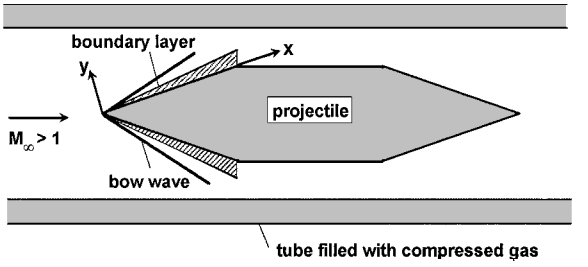

Fig. 13 Projectile flight in the compression tube.

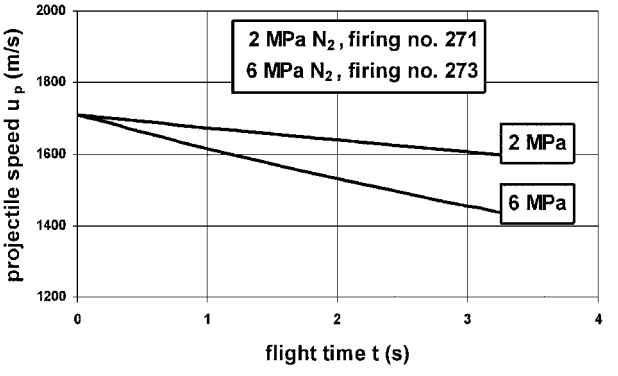

Fig. 14 Speed distribution in high-pressure test tube.

at the end of the facility, a piston is located, equipped with inner replaceable steel plates for projectile catching.

As an example for the condition in our high-pressure ground-testing facility, with a flight time of about 3 ms, the fill pressure must be higher than atmospheric pressure to model the same heat flux at the projectile cone surface as present for atmospheric air flight. With Eq. (1) we calculate for a 1-s atmospheric flight a test gas pressure of about 2 MPa or more.

Firings Performed

In our high-pressure ground-testing facility, we fired projectiles with a mass of about 150 g at a projectile speed of about 1730 m/s into the high-pressure test tube. The projectile is designed with a solid magnesium body, which is equipped with a full 28-deg steel nose cone. The projectile dimensions in millimeters are presented in Fig. 12 showing the fore-, the mid-, and the afterbody.

Test firings have been performed in a 2-MPa up to 8-MPa N_2 atmosphere with the projectile shown in Fig. 12. It is fired into the compression tube and, as mentioned, a boundary layer develops on the surface of the projectile (Fig. 13) as it develops in free flight in the atmosphere. Therefore, in the test facility, the flow around the projectile behaves similarly to atmospheric flight conditions.

Because of projectile drag, the projectile speed u_2 decreases during the flight time t_2, that is, $u_2 = u_2(t_2)$. As an example, in Fig. 14 the projectile speed diminution is shown for firing 271 in 2-MPa compressed N_2 atmosphere and for firing 273 in 6-MPa N_2. A velocity decrease of several hundred (m/s) develops that must be taken into account in the calculation of the transfer function $f_2 = f_2(u_2, t_2)$ in Eq. (1).

The nose cone temperature histories calculated for the heating during projectile flight inside of our test facility are shown in Fig. 15

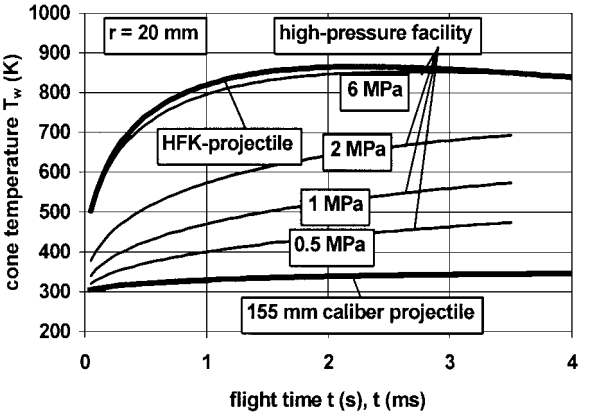

Fig. 15 Projectile nose heating in the test facility.

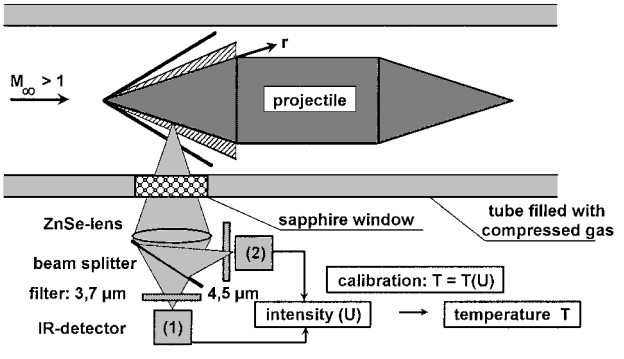

Fig. 16 Pyrometric measurement.

for filling pressures of 0.5-, 1-, 2-, and 6-MPa N_2 at $r = 20$ mm. The timescale in Fig. 15 is in milliseconds for the test-facility flight time and in seconds for the HFK and the 155-mm projectile atmospheric flight.

The outcome shows that in the case of 6-MPa N_2 in the ground-testing facility the nose temperature increase is comparable with that given for an HFK projectile. For lower cone surface temperatures, as are present in flight of a 155-mm full caliber projectile, the fill pressure in our high-pressure test tube has to be adapted to less than 0.5 MPa. In varying the fill pressure p_2, a wide range of heating scenarios can be modeled beginning at low surface temperatures at a 155-mm full caliber projectile up to high temperatures present on the surface of high-speed projectiles (Fig. 15).

Cone Surface Temperature Measurement

For surface temperature measurement, we detected the intensity of the steel surface emission at wavelengths of 3.7 and 4.5 μm. Two wavelength measurements are chosen for comparing and controlling both measurements by each other. This surface emission is registered, as outlined in Fig. 16, through a sapphire window placed near the tube end using fast infrared (IR) detectors at the time of projectile passing. The recorded output signal of the IR detector is given as voltage U vs measuring time t: $U = U(t)$. Using a calibration curve $T = T(U)$ (Ref. 2) the surface temperature T can be evaluated vs the measuring time t of projectile passage at the measuring port, that is, the sapphire window, resulting in the temperature history $T = T(t)$.

Comparison

The surface temperatures are compared, both theoretical predictions and measured, for firing 271 with 2-MPa N_2 fill pressure in Fig. 17. We used N_2 as test gas instead of air because the radiation of excited O_2 air molecules may disturb the IR emission coming from the cone surface giving a nonnegligible measuring error. N_2 molecules behave inertly, having practically the same physical gas nature as air only. The experimental result included in Fig. 17 is given for the 3.7-μm-wavelength emission.

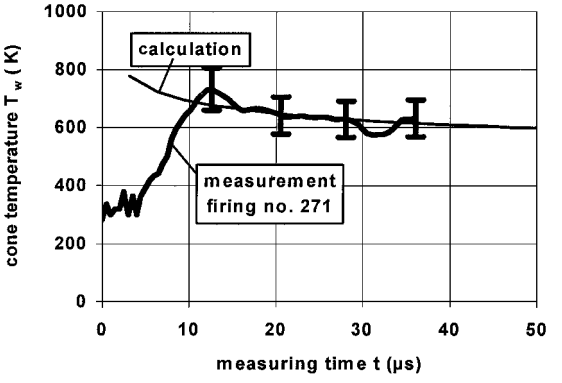

Fig. 17 Comparison for 2-MPa fill pressure.

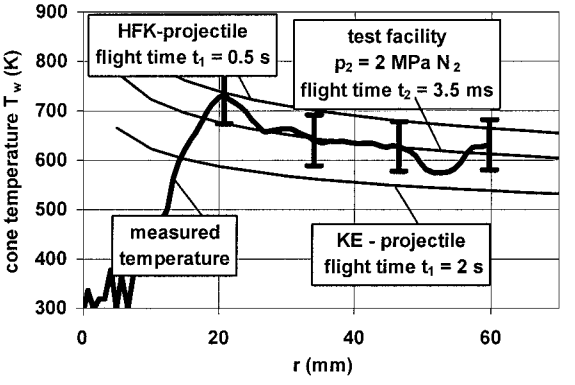

Fig. 18 Comparison of experiment and theory.

The relative measuring error (see error bars in Fig. 17) occurring for the temperature distribution is assumed to be about 10%, resulting from an analysis taking into account all of the measuring uncertainties present in our measuring device.

In Fig. 17, the measured and calculated surface temperatures are in good agreement, so that it can be assumed that the theory for predicting the temperature development at the nose of a projectile flying in our test facility can be successfully applied for predicting the projectile heating during flight in our aerothermoballistic test device. From this outcome we further assume that our theoretical model can also predict correctly the surface heating for flight scenarios in Earth atmosphere, though atmosphere pressure p_1 is lower than that in our test facility at p_2.

Adopting the fill pressure p_2 according to relation (1), the flight scenario of interest can be experimentally reproduced in our test facility, as outlined in Fig. 15. The application of the transformation law (1) established for the operation of our high-pressure testing facility can be confirmed considering the following explanations for Fig. 18, which compares the measured temperature distribution of Fig. 17 with calculated ones for real-flight scenarios. For this purpose, the direct comparison of experiment and theory as outlined for Fig. 17 is given again in Fig. 18 for fill pressure $p_2 = 2$ MPa and flight time $t_2 = 3.5$ ms. Additionally, two predicted temperature distributions are also included, which are theoretically modeled for the HFK projectile and for the KE projectile, as seen in Figs. 6–8. From this comparison, it can be concluded that in the high-pressure facility, the measured projectile surface temperature is in the range of real surface temperature histories as given during flight in Earth atmosphere (Fig. 18) for HFK projectile temperature history (flight time $t_1 = 0.5$ s) as well as for the KE projectile for a flight time $t_1 = 2$ s.

This outcome confirms that our high-pressure ground-testing facility has the capability to model the heating of a projectile during its atmospheric flight of some seconds with a flight in compressed gas of some milliseconds.

Conclusions

A ground-testing facility was designed and built for modeling the real heat transfer at the conical nose of a projectile flying in

the atmosphere. In this facility, the projectile is traveling through a compressed gas to obtain within some milliseconds the same surface heating as present during an atmospheric flight of some seconds. To date this high-pressure facility is unique worldwide for modeling this phenomenon. Using the similarity law (1), the heating for the flight of some seconds t_1 in the atmosphere at pressure p_1 and that for the model flight time of some milliseconds t_2 in the test tube at a higher pressure p_2 are equal if relation (1) is applied for determination of pressure p_2 for modeling a desired flight scenario.

For calculating the temperature distribution at the surface, it is assumed that a compressible and turbulent boundary-layer develops at the conical projectile nose surface behind the bow wave. Using Prandtl's boundary-layer equations of mass, momentum, and energy, a theoretical model has been developed to calculate the boundary-layer development, as well as the heat flux from gas to surface. Using an analytical solution resulting from the heat conduction equation, the temperature distribution at the cone surface and in depth is calculated. This procedure is based on the similarity of cone and plate boundary layer. Herein, the solution for the heat flux from the plate boundary layer is used and transformed to that on the conical nose of a projectile.

We investigated the projectile nose heating using an aerothermoballistic high-pressure test facility for a 30-mm caliber. Special projectiles are accelerated to velocities up to about 1700 m/s, flying in compressed nitrogen at gas pressures of 2 MPa and more. The compression tube used has a length of about 5 m with an inner two-caliber bore. The outer caliber is 44 mm and the inner rail caliber is 30 mm for projectile guiding. To measure the surface temperature, we look for the surface emission at wavelengths of about 3.7 and 4.5 μm, respectively. This surface emission is registered through a sapphire window placed near the test tube muzzle using fast IR detectors at the time of projectile passing: $U = U(t)$. The surface temperature T is given by a calibration function $T = T(U)$ as a function of the surface emission.

Experiment 271 with 2-MPa fill pressure shows the good applicability of the theoretical procedure for predicting the cone boundary-layer formation. Furthermore, the capability of our aerothermoballistic test facility to model the temperature distribution along the projectile's nose cone as compared with atmospheric flight cycles, for example, HFK projectile flight or the flight of a KE projectile was explained. Summarizing, real surface temperature histories arising during atmospheric flight are modeled and obtained in our test facility, as outlined for some typical flight scenarios using actual projectile types.

Acknowledgments

The idea for modeling the heating process on the nose of a projectile during its atmospheric flight was first discussed by Günter Smeets, former scientist at the French–German Research Institute of Saint-Louis (ISL), retired since 1999. The authors thank G. Smeets for his helpful contributions during the design and building of our test facility. Furthermore, the authors would like to express their gratitude to Hans Mach, also retired from ISL since 1999, for the suggestion and the development of the pyrometric measuring technique used herein and for many fruitful discussions on this topic during his scientific work at ISL.

References

[1] Schlichting, H., and Gersten, K., *Boundary-Layer Theory*, Springer-Verlag, 8th ed., 2000, Pt. 4.

[2] Seiler, F., Mach, H., Werner, U., Patz, G., and Smeets, G., "Theoretical and Experimental Investigation of Bow Wave Heating at the Conical Nose of Projectiles," *Proceedings of the 22nd International Symposium on Shock Waves*, Imperial College, London, July 1999.

[3] Hantzsche, W., and Wendt, H., "Die laminare Grenzschicht bei einem mit Überschallgeschwindigkeit angeströmten nichtangestellten Kreiskegel" ("The Laminar Boundary Layer on a Spherical Cone in Hypersonic Flow at Zero Incidence"), *Jahrbuch der deutschen Luftfahrtforschung I*, 1960.

[4] Chien, K.-Y., "Hypersonic, Turbulent Skin-Friction and Heat-Transfer Measurements on a Sharp-Cone," *AIAA Journal*, Vol. 12, No. 11, 1974.

[5] Oertel, H., *Stoßrohre* (*Shock Tubes*), Springer-Verlag, 1st ed., 1966, Chap. B.8.4, p. 355.

[6] Seiler, F., "Theoretische und experimentelle Untersuchüng der turbulenten Grenzschicht hinter einem Kolben im Stoßrohr" ("Theoretical and Experimental Investigation of the Turbulent Boundary Layer Behind a Piston in the Shock Tube"), French–German Research Inst. of Saint Louis, ISL Rept. 115/93, Saint-Louis, France, 1993.

[7] Gnemmi, P., Sommer, E., Naumann, K.W., and Fleck, V., "Aerothermal Study of a Projectile in Flight: Experiment–Computation Comparison," *Proceedings of the 18th International Symposium and Exhibition on Ballistics*, San Antonio, TX, Nov. 1999.

[8] Seiler, F., Gatau, F., and Mathieu, G., "Prediction of Surface Heating of a Projectile Flying in RAMAC 30 of ISL," *Proceedings of the 3rd International Workshop on Ram Accelerators, RAMAC III*, Tohoku Univ., Sendai, Japan, July 1997.

T. C. Lin
Associate Editor